




Fabrication and performance improvement of Ag grid transparent conducting films using selective laser ablation

Qian Xu^{1,4}, Bao-jia Li^{1,2,4,*} , Li-jing Huang^{2,3,4,*}, Huang Li^{1,4}, and Yong-ying Wang^{1,4}

¹School of Materials Science and Engineering, Jiangsu University, Zhenjiang 212013, People's Republic of China

²Institute of Micro-Nano Optoelectronic and Terahertz Technology, Jiangsu University, Zhenjiang 212013, People's Republic of China

³School of Mechanical Engineering, Jiangsu University, Zhenjiang 212013, People's Republic of China

⁴Jiangsu Provincial Key Laboratory of Center for Photon Manufacturing Science and Technology, Jiangsu University, Zhenjiang 212013, People's Republic of China

Received: 4 October 2021

Accepted: 25 December 2021

Published online:

4 January 2022

© The Author(s), under exclusive licence to Springer Science+Business Media, LLC, part of Springer Nature 2022

ABSTRACT

Silver (Ag) grid transparent conducting films (TCFs) were firstly fabricated by selective laser ablation of Ag thin films prepared by radio frequency magnetron sputtering under the conventional scanning method (i.e., line-typed cyclic scanning, LTCS). The effects of grid parameters (i.e., Ag grid height, pitch, and line-width) on TCF morphology, optical transmittance, electrical conductivity, and comprehensive performance were studied. The optimal Ag grid height, pitch, and line-width were determined to be 800 nm, 1.0 mm, and 90 μm , respectively, and the resulting TCF showed a figure of merit of $11.38 \times 10^{-2} \Omega^{-1}$. Subsequently, two new scanning methods, i.e., frame-typed serial scanning (FTSS) and frame-line combined scanning (FLCS), were adopted to further optimize the fabrication process, and thus the TCF comprehensive performance. The results showed that as compared to the LTCS method, the FTSS and FLCS methods could effectively eliminate semicircular-shaped Ag grid line edges, and thus obtain relatively smooth and flat ones without obvious Ag material residues. The Ag grid TCF fabricated by using the FLCS method had the highest figure of merit of $13.02 \times 10^{-2} \Omega^{-1}$, indicating a further improvement in comprehensive performance.

Address correspondence to E-mail: li_bjia@126.com; lij_huang@126.com

1 Introduction

Transparent conducting film (TCF) is a kind of photoelectric material which combines optical transparency and electrical conductivity. It has been widely used in optoelectronic devices, such as solar cells [1, 2], touch screens [3], liquid crystal displays [4], windshield heaters [5], and light-emitting diodes [6]. In particular, the TCF is an indispensable part of a solar cell. As the window material of the solar cell, the TCF must have an excellent comprehensive performance with high optical transparency and low sheet resistance to meet the application requirements, so its properties directly determine the performance of the solar cell in a sense. The main materials used for the TCF are metal oxides [7, 8], carbon-based materials [9], metal nanowires [10], and metal grids [11]. Indium tin oxide (ITO) is the main metal oxide used for the TCF, and its production process is mature. ITO film is widely used as a TCF in the optoelectronics industry and requires a low sheet resistance (as low as $8 \Omega/\text{sq}$) and a high optical transmittance in the visible waveband (above 80% as average value) to meet the application requirements [12, 13]. However, the preparation of ITO requires the use of the rare and toxic metal indium, which leads to a high production cost and restricts its applications [14, 15]. The ITO film itself also has a certain brittleness that makes it difficult to be used in flexible devices [16]. Carbon nanotubes (CNTs) have good mechanical properties and are excellent to replace ITO, but the large contact resistance between each single CNT limits their applications as transparent conducting layers [17]. The preparation methods of metal nanowires are simple and suitable for large-scale production [18]. Kim et al. [19] prepared silver (Ag) nanowires on flexible polycarbonate (PC) substrates by electrostatic spray deposition, and found that the optical transmittance of the Ag nanowire TCF was inversely proportional to the haze. In order to reduce the haze and maintain the good electrical conductivity of the TCF, it is necessary to extend the lengths of the nanowires. Unfortunately, it is difficult to prepare Ag nanowires with large aspect ratios.

In recent years, metal grids have attracted much attention due to their excellent optical and electrical properties. Metal grids are commonly prepared by adopting Ag, copper (Cu), and other metal materials to form transparent and conducting metal network-like patterns on glass or plastic substrates [11, 16, 20].

The network-like patterns can be designed as arrays of different graphical structures, and the grid line-width and pitch can be easily controlled to adjust the electrical conductivity and optical transmittance of the resulting metal grid TCF. There are many preparation methods for metal grids, mainly including lithography [21], nanoimprinting [22], crackle template [23], and inkjet printing [24]. At present, these commonly used methods suffer from some problems. For example, some methods need to introduce mask, template, or metal nanoparticle ink, while the preparation processes of the mask, template, and metal nanoparticle ink are usually complex, and certain sizes of metal nanoparticles are even required in some cases [16]. These greatly increase the preparation cost. The crackle template method also has the disadvantages of uncontrollable grid distribution and nonadjustable structure size. Consequently, laser direct writing techniques including selective laser sintering (SLS) [25] and selective laser ablation (SLA) [26] have been developed to prepare metal grid TCFs. Actually, the SLS method also requires the expensive and certain-sized metal nanoparticle ink. By contrast, the SLA method is simpler, more flexible, and less costly, and the performances of the metal grid TCF prepared by SLA can be directly adjusted by varying laser parameters [27]. During SLA, the precise removal of a metal layer with a controllable ablation depth (i.e., metal grid height) along a preset network-like pattern can be achieved by reasonably controlling the laser parameters. Paeng et al. [28] carried out SLA on a 19-nm-thick Cu film, and successfully prepared a circular-hole-arrayed Cu TCF with an optical transmittance of 83% at the wavelength of 550 nm and a sheet resistance of $17.48 \Omega/\text{sq}$. It should be noted that the grid shape, size, and quality of the TCF obtained by their method are mainly limited by the laser spot [29]. Generally, the shape of the metal grid TCF obtained by this method is single and has a larger coverage area, thus resulting in performances that are just close to those of the commercial ITO film on the market and need a further optimization. In addition, Jia et al. [30] combined the laser ablation method and the numerical control processing technology, and successfully achieved the localized fine removal with flat edges and small heat-affected zones along three-dimensional patterns for Cu coatings on polyimide (PI) substrates. Inspired by their studies, it is expected that by controlling the structure sizes and quality of

laser-ablated patterns, the performances of the obtained metal grid TCF can be effectively improved. Actually, our group has previously carried out a preliminary study about width and depth control [27] as well as edge quality improvement [31] of laser-ablated grooves on Ag films, based on which the optimal laser processing parameters (i.e., laser fluence, defocusing amount, and scanning speed) and scanning method for laser ablation have been determined. However, a further systematical investigation about the fabrication of Ag grid TCFs by the SLA method has not been performed, and the grid parameter and scanning method influences on the resulting TCF performances have not been addressed yet.

In this work, the Ag films deposited on glass substrates by radio frequency (RF) magnetron sputtering were precisely removed by SLA along pre-designed square grid array patterns, so as to fabricate Ag grid TCFs. The SLA method gave rise to the possibility for obtaining controllable grid structure sizes. The grid parameters, i.e., Ag grid height, grid pitch, and grid line-width, were studied for optimization under the conventional line-by-line round-trip cyclic scanning method (i.e., line-typed cyclic scanning, LTCS [32]). Subsequently, the two new scanning methods proposed in our previous work [31], i.e., frame-typed serial scanning (FTSS) and frame-line combined scanning (FLCS), were adopted for further optimizing the fabrication process of the Ag grid TCFs. The FTSS and FLCS methods were actually beneficial to improving the edge quality of the laser-removed areas during SLA, and thus the optical transmittance and electrical conductivity of the resulting Ag grid TCFs. The effects of grid parameters and scanning methods on morphology, optical transmittance, electrical conductivity, and comprehensive performance of the obtained Ag grid TCFs were systematically analyzed. Comparing the results of the FTSS and FLCS methods with those of the conventional LTCS method can provide new insights into the performance improvement of metal grid TCFs fabricated by SLA.

2 Experimental details

Figure 1 shows the process flowchart for fabricating Ag grid TCFs using the SLA method. The commercial soda–lime float glass with a size of 15 mm × 15

mm × 1 mm (Shenzhen Nuozhuo Technology Co., Ltd., China) was selected as the substrate. Before RF magnetron sputtering, the glass substrate was successively placed in deionized water, acetone, and anhydrous ethanol to perform ultrasonic cleaning under room temperature and a power of 50 W. The time for each cleaning process was controlled at 10 min. After ultrasonic cleaning, the glass substrate was dried by blowing high-purity (99.999%) nitrogen gas, and then kept in the oven at 50 °C for 2 h for further drying. After natural cooling, the glass substrate was taken out, and then an Ag film with a certain thickness (500–900 nm) was deposited on it by an RF magnetron sputtering coating system (Hefei Kejing Materials Technology Co., Ltd., VTC-2RF, China) at room temperature. Before sputtering the Ag film, the sputtering chamber was vacuumized by a rotary vacuum pump to a base pressure of 4 Pa, and then injected high-purity (99.999%) argon gas as the sputtering gas to a pressure of 100 Pa maintaining 5 min to further expel the air from the chamber. During sputtering, a commercial circular Ag plate with a diameter of 50 mm, a thickness of 4 mm and a purity of 99.99% (Zhongnuo Advanced Material (Beijing) Technology Co., Ltd., China) was used as the sputtering target. The sputtering power, the working pressure, the rotation speed of the sample stage and the distance between the target and the substrate were fixed at 30 W, 15 Pa, 4 r/min and 50 mm, respectively. The thickness of the Ag film (corresponding to the Ag grid height) was monitored by a quartz-crystal-based thickness monitor equipped on the coating system and observed through a computer monitor connected to the coating system. Subsequently, the as-prepared Ag film was subjected to SLA using a diode pumped Nd:YVO₄ nanosecond pulsed laser (Bright Solutions Co., Ltd., Wedge532, Italy), which had a center wavelength of 532 nm, a pulse width of 1–2 ns, a pulse repetition frequency of 1 kHz and a maximum single pulse energy of 0.9 mJ.

Figure 2 shows schematic diagram of the nanosecond pulsed laser ablation system. The laser beam was firstly emitted by the nanosecond pulsed laser and then vertically irradiated on the surface of the sample after passing through the beam expander, total reflector, vibration mirror system, and focusing lens. The sample was placed on the X–Y moving stage, which could realize two-dimensional motions under the control of the computer. The laser parameters and scanning paths could also be preset and

Fig. 1 Flowchart of the process to fabricate Ag grid TCFs through selective laser ablation

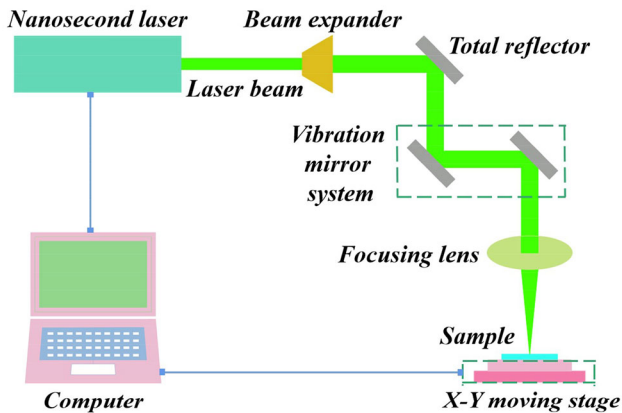
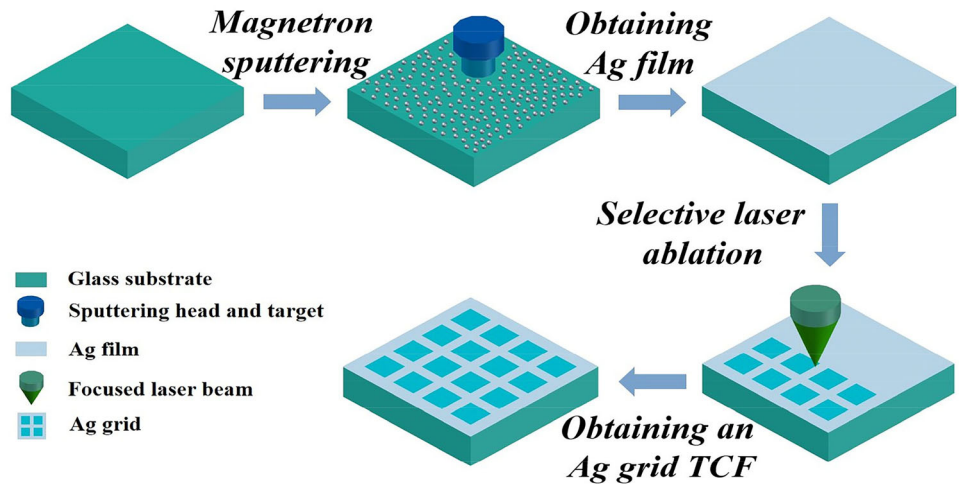


Fig. 2 Schematic diagram of the nanosecond pulsed laser ablation system

controlled by the program in the computer. After SLA, the sample was taken off from the X–Y moving stage and gently blown with a washing ear ball to remove the laser ablation-caused spatters on its surface.

Our previous work has addressed the variation of laser-ablated groove width and depth on an Ag film with laser fluence and defocusing amount under a single scan, and the result has showed that the Ag film can be removed without damaging the glass substrate under a moderate laser fluence and defocusing amount [27]. Also a large number of previous experiments have determined that the most appropriate scanning speed for laser-ablated groove with good edge quality was 15 mm/s [31]. According to these results, the laser fluence, defocusing amount, and scanning speed in this present work were, respectively, controlled to be 0.8 J/cm², 1.0 mm, and 15 mm/s, and the selective removal of the Ag film

was realized by layer-by-layer laser scanning during SLA. Under these parameter conditions, the single laser ablation line-width was found to be about 130 μm. Figure 3 presents the schematic diagram of the Ag grid array fabricated by SLA. The laser beam followed the cyan lines to ablate the Ag film and thus form the square removed areas, and the unremoved areas constituted Ag grid lines. As Fig. 3 shows, d_1 represents the scan line spacing (i.e., the distance between two adjacent laser ablation tracks), d_2 represents the Ag grid line-width (i.e., the distance between two adjacent removed areas), and d_3 represents the Ag grid pitch (i.e., the side length of a single square removed area). In order to obtain a better removal effect of the Ag film, the d_1 value was fixed at 50 μm based on the previous experimental results [31]. The fabrication of Ag grid TCFs with adjustable performances could be realized by varying the d_2 and d_3 values.

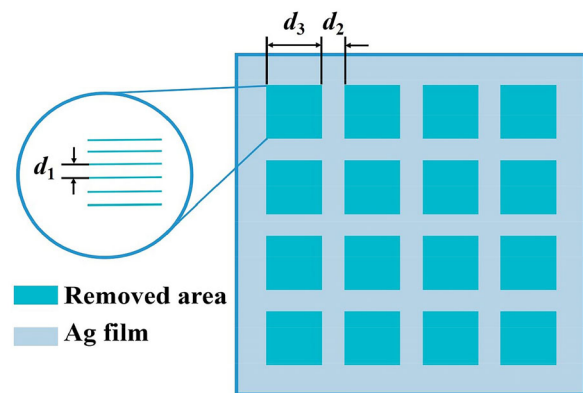


Fig. 3 Schematic diagram of the Ag grid array fabricated by selective laser ablation

The surface morphology characterizations of the fabricated Ag grid TCFs were performed using a scanning electron microscope (SEM) (Carl Zeiss Co., Ltd., EVO MA10, Germany). The optical transmittance spectra of the Ag grid TCFs were measured by a UV–Vis spectrophotometer (Shanghai Metash Instruments Co., Ltd., UV-8000, China). The sheet resistance values of the Ag grid TCFs were tested through a digital four-point probe instrument (Guangzhou 4-Probes Technology Co. Ltd., RST-9, China).

3 Results and discussion

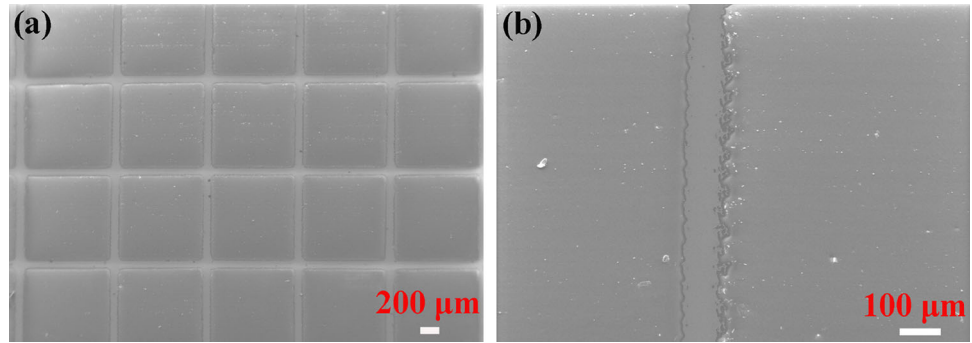
3.1 Influence of grid height

It has been reported that the metal layer thickness has a significant effect on the optical and electrical properties of the metal grid TCF [27, 33]. By increasing the thickness of the metal layer, the electrical conductivity of the metal grid TCF can be improved as much as possible on the basis of slightly reducing the optical transmittance, so as to realize an effective improvement in comprehensive performance of the TCF [34]. Based on this, the Ag grid line-width (d_2) and pitch (d_3) were, respectively, fixed at 90 μm and 1.0 mm, and the conventional LTCS method was adopted to study the influence of Ag grid height (i.e., Ag film thickness) on the as-prepared Ag grid TCFs. The Ag grid heights were 500, 600, 700, 800, and 900 nm, respectively. Our previous work has confirmed that single-scan laser ablation using the same laser parameters can only realize complete removal of a 100-nm-thick Ag film, and the removed layer thickness (i.e., laser-ablated groove depth) is linearly increased with the increase in scanning number [27]. Therefore, in this present work, the layer-by-layer laser scanning for completely removing the Ag films with thicknesses of 500–900 nm required scanning numbers of 5–9.

Figure 4 shows the low-magnification and partially enlarged SEM images of the Ag grid TCF with a grid height of 800 nm. The single change in Ag grid height was found to result in a similar surface morphology, and therefore the SEM images of the other Ag grid TCFs are not provided here. It could be seen from Fig. 4a that after SLA, a clear grid structure composed of Ag film was formed on the glass substrate. There were no obvious Ag material residues in the

laser-removed areas, which indicates that the Ag film can be selectively removed from the substrate by laser ablation [35, 36]. In our previous work [27], it has been indicated that the mechanism for complete laser removal of a 100-nm-thick Ag film by single-scan laser ablation using the same laser parameters as this present work can be explained by laser-induced thermoelastic force. This is because the laser energy per unit area irradiated on the Ag film is enough to generate a thermoelastic force that exceeds the film cohesion and the film-to-substrate adhesion, and thus can realize thermal–elastic removal of the film without obvious Ag residues. It has been also reported that when the Ag film is very thick (e.g., 400 or 500 nm in thickness), the laser-induced thermal diffusion length will be much smaller than the Ag film thickness, and therefore the whole Ag film cannot be heated under a single-scan laser ablation to generate a sufficiently strong thermoelastic force [37, 38]. In this case, the main mechanism of laser removal is partial vaporization of the film material. Specifically, the laser energy is firstly absorbed by free electrons in the Ag film, and then transferred to the lattice through electron–phonon (lattice) coupling. Laser ablation will occur when the lattice temperature is higher than the melting point of the Ag film, and then the Ag film will be molten and vaporized [39]. In the vaporization process, there will be some Ag residues due to Gaussian distribution of the laser energy [40]. In this present work, the Ag film is very thick (≥ 500 nm in thickness) and requires multiple-scan laser ablation (≥ 5 in scanning number) for complete removal. It is worth noting that multiple-scan laser ablation of the Ag film is from top to bottom with a removal depth per scan of about 100 nm. Therefore, it can be inferred that the removal mechanism of the first few scans is mainly the partial vaporization of the Ag film caused by laser ablation. Considering the adhesion between the remaining thinner Ag film and the substrate, the removal mechanism of the last few scans should include partial vaporization and thermal–elastic removal of the Ag film. In order to further study the removal effect and the quality of the Ag grid lines after SLA, part of the area in Fig. 4a was selected and enlarged to obtain Fig. 4b. A clear observation from Fig. 4b was that the width of the Ag grid line obtained under this condition was about 90 μm . In addition, both edges of the Ag grid line were semicircular, and there were some Ag residues around the edges of the Ag grid line. The projection

Fig. 4 SEM images of the Ag grid TCF with a grid height of 800 nm: **a** a low-magnification view; **b** a partially enlarged view



of laser spot and the Gaussian distribution of laser energy may be the main reasons for this phenomenon [40]. Since the start and end areas of the laser scanning path are semicircular as a result of laser spot projection, it is easy to know that the edges of the Ag grid lines obtained under the conventional LTCS method will usually be semicircular [31, 41]. The Ag material residues at the edges of the Ag grid lines are believed to be resulted from the Gaussian distribution of the laser pulses, which makes the laser energy in the edge areas smaller. Detailedly, this smaller laser energy can result in partial vaporization removal of the Ag film at the edges of the laser-ablated regions, and thus the unremoved Ag film materials will be remained to be inevitably turned into Ag residues. These Ag residues certainly have some impacts on the properties of the resulting Ag grid TCF, which will be discussed later.

Figure 5a presents the optical transmittance spectra of the Ag grid TCFs with different grid heights within the wavelength range of 250–900 nm. It was found that the optical transmittance of the Ag grid TCFs

decreased with the increase of Ag grid height, which should be ascribed to the well-known fact that the thicker Ag film can cause more light scattering and reflection losses. It could also be seen that all the TCFs achieved the maximum transmittance at the wavelength around 600 nm. This may be resulted from the higher light absorption in the short-wavelength region and the higher light reflectance/scattering in the long-wavelength region of the Ag material (i.e., selective light transmission of Ag) [42]. In order to reflect the change trend of the optical transmittance more visually, the average transmittance (T_{av}) values of the Ag grid TCFs in the visible waveband of 380–780 nm were calculated using the following formula [43].

$$T_{av} = \frac{\sum_{i=1}^n T_i}{n}, \tag{1}$$

where T_i is the measured value of optical transmittance at a given wavelength, and n is the number of the measured optical transmittance values within the calculated wavelength range. Figure 5b displays the

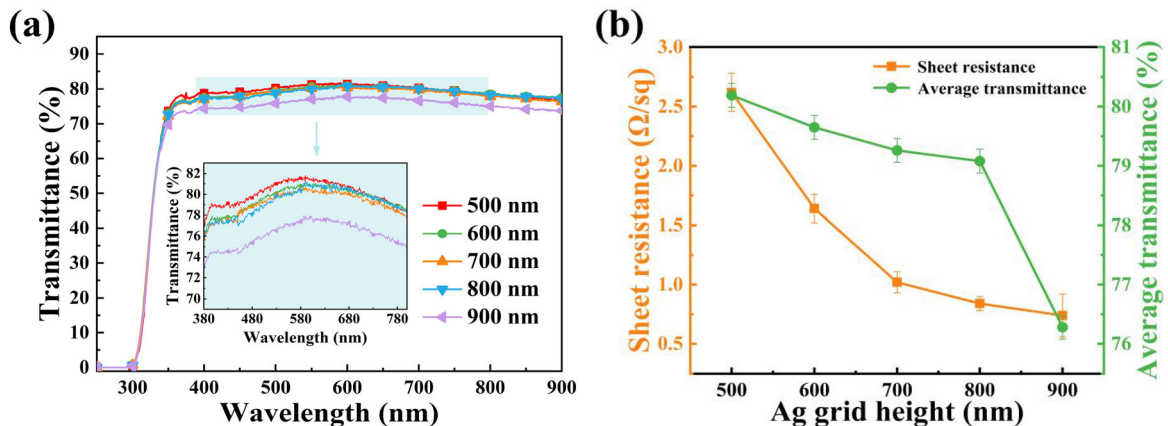


Fig. 5 **a** Optical transmittance spectra and **b** sheet resistance and average transmittance values of the Ag grid TCFs with different grid heights. The inset in **a** shows the optical transmittance spectra of the Ag grid TCFs in the visible waveband of 380–780 nm

calculated average transmittance values of the Ag grid TCFs with different grid heights. It could be observed that the Ag grid TCF with a grid height of 500 nm had the highest average transmittance of 80.19%, and the decrease rate of the average transmittance was relatively gentle with the increase in grid height from 500 to 800 nm. When the grid height reached 900 nm, the average transmittance remarkably dropped to the lowest value of 76.28%. This should be attributed to the strong scattering and reflection effects of Ag on the incident light. With the increase of Ag grid height, the light scattering and reflection losses from the Ag grid were gradually enhanced [44], and thus the average transmittance was gradually decreased. The similar result has also been reported by Khan et al. [45]. The average transmittance was found to be decreased by about 4% as the grid height increased from 500 to 900 nm.

Figure 5b also provides the measured sheet resistance values of the Ag grid TCFs with different grid heights. It could be seen that the sheet resistance of the Ag grid TCF with a grid height of 500 nm was 2.62 Ω/sq , and the sheet resistance exhibited a gradually decreasing trend with the increase of grid height. When the grid height was 900 nm, the sheet resistance was decreased to the lowest value of 0.74 Ω/sq . The sheet resistance (R_{sh}) of a square metal grid TCF can be determined by the following expression proposed by Van de Groep et al. [46].

$$R_{\text{sh}} = \frac{\rho}{d} \cdot \frac{l}{b}, \quad (2)$$

where ρ represents the resistivity of the metal material, d is the metal grid height, l is the metal grid pitch, and b is the metal grid line-width. Here, the ρ , l , and b values are fixed, and therefore the R_{sh} value of the Ag grid TCF is inversely proportional to the Ag grid height d according to Eq. (2). Certainly, the R_{sh} value of the Ag grid TCF will also be affected by the enhanced uniformity and compactness of the original Ag film caused by the increase in thickness, because the film with enhanced uniformity and compactness is more conducive to the transmission of electrons [47]. The gradual decrease in sheet resistance with the increase of grid height for the Ag grid TCFs can thus be understood.

From the above analyses, it was noticed that the increase in grid height resulted in decreased optical transmittance but enhanced electrical conductivity for the Ag grid TCFs. This indicates that there is a

trade-off between optical transmittance and electrical conductivity. In order to compare and evaluate the comprehensive performances of the Ag grid TCFs more reasonably, the concept of figure of merit (F_{TC}) was introduced with the calculation formula defined by Haacke [48] as

$$F_{\text{TC}} = \frac{T_{\text{av}}^{10}}{R_{\text{sh}}}. \quad (3)$$

The higher the F_{TC} value, the better the comprehensive performance [49]. The calculated F_{TC} values of the Ag grid TCFs with different grid heights are given in Fig. 6. It was found that with the increase in Ag grid height, the F_{TC} value was increased at first and then decreased. The Ag grid TCF with an Ag grid height of 800 nm had the highest F_{TC} value of $11.38 \times 10^{-2} \Omega^{-1}$, which is 2.7 times that of the Ag grid TCF with an Ag grid height of 500 nm ($4.19 \times 10^{-2} \Omega^{-1}$). In general, under the same other conditions, using an Ag grid height of 800 nm enables fabrication of an Ag grid TCF with the best comprehensive performance.

3.2 Influence of grid pitch

The Ag grid pitch (i.e., d_3 in Fig. 3) can be adjusted by reasonably setting the side length of the single square removed area during SLA [19]. In order to study the effect of Ag grid pitch, the optimal Ag grid height of 800 nm was employed, the Ag grid line-width (d_2) was fixed at 90 μm , and the conventional LTCS method was adopted. The Ag grid pitches were 0.4, 0.7, 1.0, 1.3, and 1.6 mm, respectively.

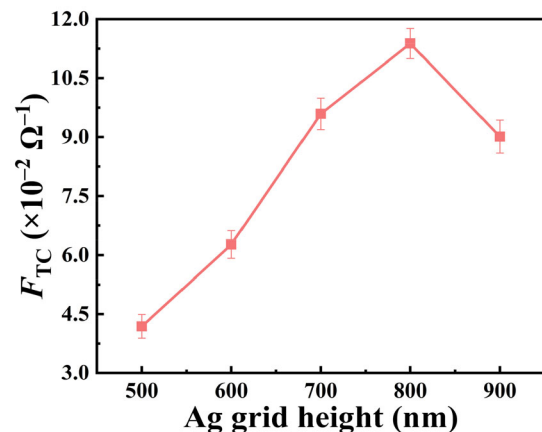


Fig. 6 Figure of merit (F_{TC}) values of the Ag grid TCFs with different grid heights

Fig. 7 SEM images of the Ag grid TCFs with different grid pitches: **a** 0.4 mm; **b** 0.7 mm; **c** 1.3 mm; **d** 1.6 mm

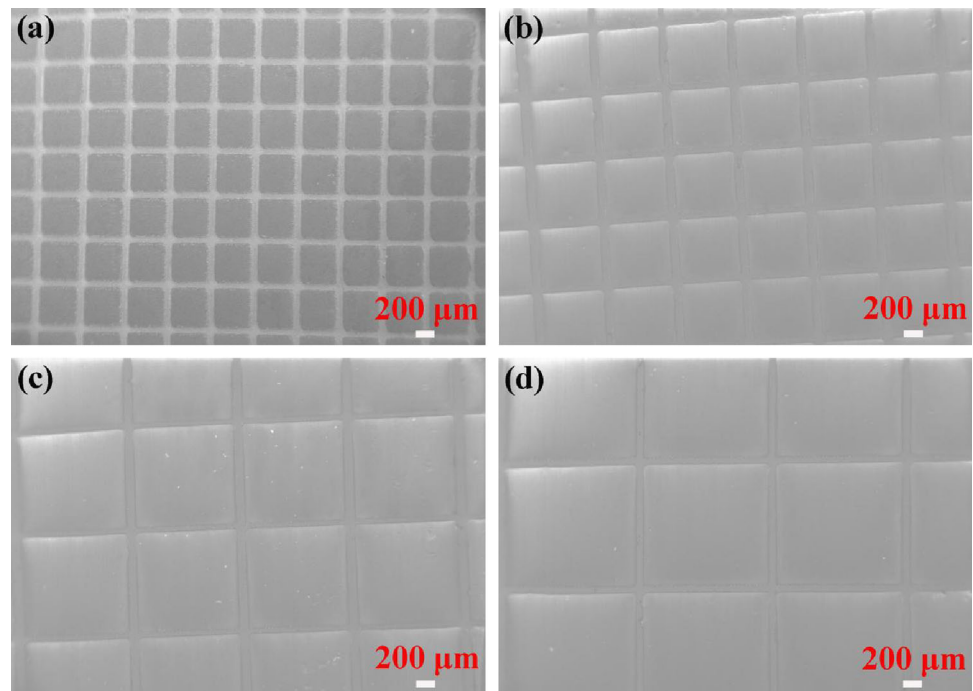


Figure 7 shows the SEM images of the Ag grid TCFs with different grid pitches. Regular Ag grid structures without obvious Ag material residues in the removed areas could be found on all the TCF sample surfaces. Combined with Fig. 4a for the Ag grid TCF with a grid pitch of 1.0 mm, it could be observed that the increase in Ag grid pitch led to unobvious changes in Ag grid line-width but gradually decreases in the number of Ag grid lines per unit area. This means that the content of Ag material per unit area was gradually reduced. On the one hand, since the Ag film itself has strong scattering and reflection effects on the incident light [50], the reduction of the Ag material content will undoubtedly lead to an increase in optical transmittance of the Ag grid TCF. On the other hand, the decrease of the Ag material content per unit area will inevitably cause a degradation in electrical conductivity for the Ag grid TCF, as confirmed by the results of Jang et al. [51]. The related discussions will be performed later.

Figure 8a presents the optical transmittance spectra of the Ag grid TCFs with different grid pitches within the 250–900 nm waveband. It could be seen that unlike the grid height, the increase in grid pitch resulted in a significant enhancement in optical transmittance of the Ag grid TCFs. This should be explained by the phenomenon that increased grid pitch can result in a decreased Ag grid line number

(i.e., Ag material content) per unit area to reduce the light scattering and reflection losses from Ag [52]. The average transmittance values of the Ag grid TCFs with different grid pitches in the visible waveband of 380–780 nm were also calculated using Eq. (1), and the results are displayed in Fig. 8b. When the Ag grid pitch was 0.4 mm, the average transmittance of the Ag grid TCF was only 67.18%. With the increase of Ag grid pitch, the average transmittance was increased gradually. As the Ag grid pitch reached 1.6 mm, the average transmittance of the Ag grid TCF was increased to the largest value of 82.78%. As mentioned above, the change of the Ag grid line number per unit area should be responsible for these results [50]. Specifically, the scattering and reflection of the incident light that resulted from the Ag grid pattern will bring about a certain loss of optical transmittance [53], and the increased Ag material content can usually lead to enhanced light scattering and reflection [54]. Since the larger Ag grid pitch corresponded to a lower Ag material content per unit area, the light scattering and reflection effects were weakened, and thus the average transmittance of the Ag grid TCFs exhibited an increasing trend with the increase of Ag grid pitch.

Figure 8b also provides the measured sheet resistance values of the Ag grid TCFs with different grid pitches. It could be clearly observed that the change

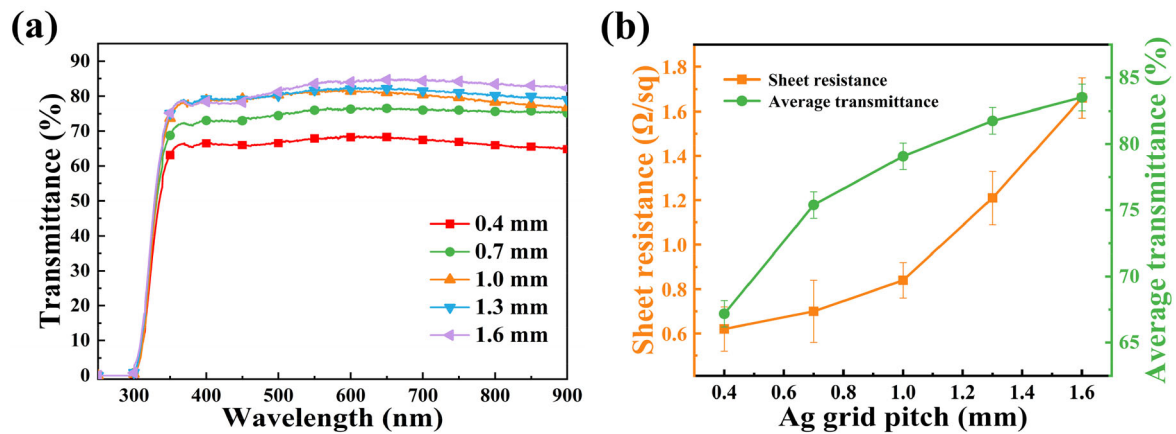


Fig. 8 **a** Optical transmittance spectra and **b** sheet resistance and average transmittance values of the Ag grid TCFs with different grid pitches

trend of the sheet resistance was the same as that of the optical transmittance, that is, gradually increasing with the increase of Ag grid pitch. The Ag grid TCF with a grid pitch of 0.4 mm had the lowest sheet resistance of 0.62 Ω/sq , and that with a grid pitch of 1.6 mm had the largest one of 1.66 Ω/sq . These results should also be ascribed to the change of the Ag grid line number per unit area. The above SEM analysis revealed that the increase in Ag grid pitch gave rise to a decrease in Ag grid line number per unit area but nearly no change in Ag grid line-width. Therefore, the Ag material content per unit area reduced, resulting in gradually degraded electrical conductivity of the Ag grid TCFs. Jeong et al. [55] have also reported similar results. Actually, according to Eq. (2), with the unchanged ρ , d , and b values, the sheet resistance (R_{sh}) value of the Ag grid TCF is directly proportional to the Ag grid pitch (l), which can also reasonably explain the results in this present work.

Based on the above analyses, it is known that although increasing Ag grid pitch can effectively improve the TCF optical transparency, it will cause a significant deterioration of the TCF electrical conductivity. Therefore, the F_{TC} values of the Ag grid TCFs with different grid pitches were also calculated using Eq. (3) for comparing and evaluating their comprehensive performances, and the results are given in Fig. 9. The F_{TC} values exhibited a trend of increasing firstly and then decreasing with the increase in Ag grid pitch. The Ag grid TCF with an Ag grid pitch of 1.0 mm had the highest F_{TC} value of $11.38 \times 10^{-2} \Omega^{-1}$. Compared with the Ag grid TCF with an Ag grid pitch of 0.4 mm that had the lowest

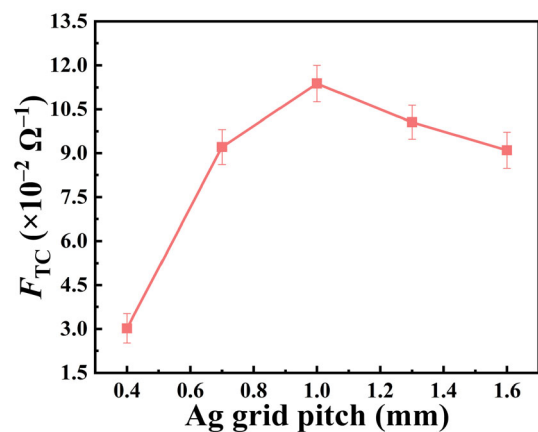


Fig. 9 Figure of merit (F_{TC}) values of the Ag grid TCFs with different grid pitches

F_{TC} value of $3.02 \times 10^{-2} \Omega^{-1}$, the F_{TC} value was enhanced by nearly 3.8 times. The results indicate that under the same other conditions, the optimal Ag grid pitch for fabricating an Ag grid TCF with the best comprehensive performance is 1.0 mm.

3.3 Influence of grid line-width

The Ag grid line-width (i.e., d_2 in Fig. 3) can be adjusted by reasonably setting the distance between two adjacent removed areas during SLA [20]. In order to explore the effect of Ag grid line-width, the optimal Ag grid height of 800 nm and grid pitch of 1.0 mm were employed, and the conventional LTCS method was adopted. The Ag grid line-widths were 70, 80, 90, 100, and 110 μm , respectively.

Figure 10 shows the SEM images of the Ag grid TCFs with different grid line-widths. Similarly, the

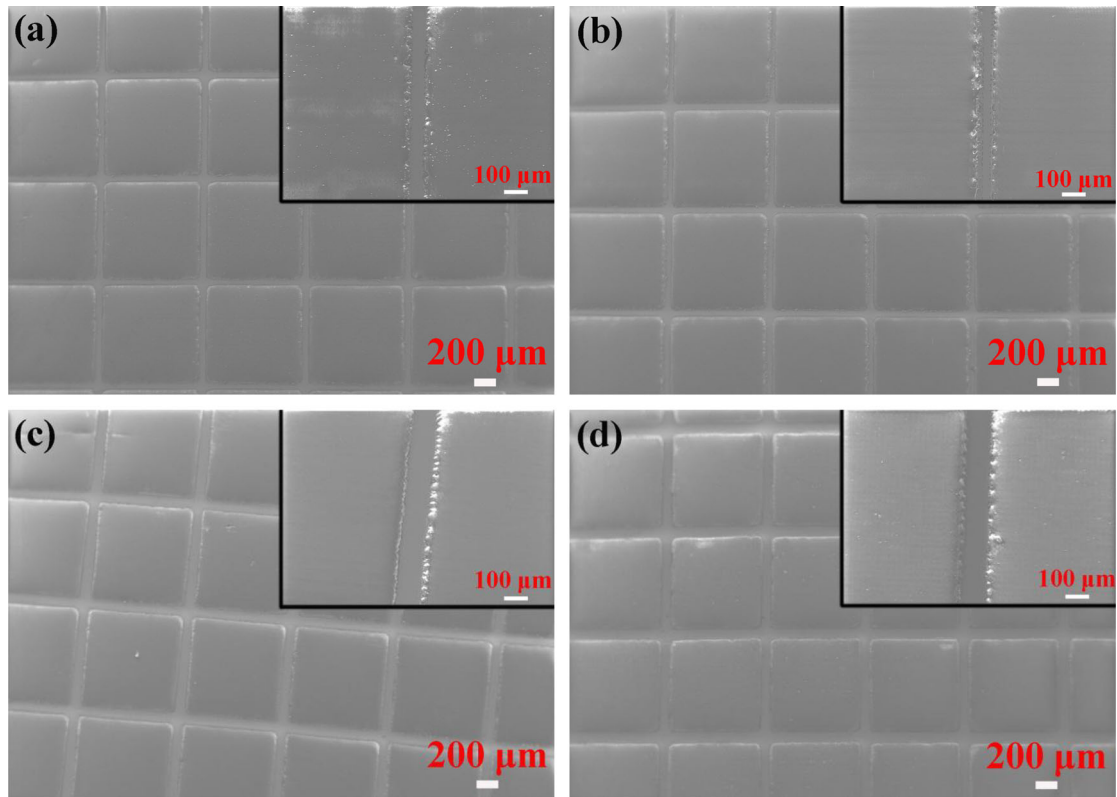


Fig. 10 SEM images of the Ag grid TCFs with different grid line-widths: **a** 70 μm ; **b** 80 μm ; **c** 100 μm ; **d** 110 μm . The insets show partially enlarged SEM images of the corresponding Ag grid TCFs

surfaces of all the samples were covered with clear and regular Ag grid structures, and no obvious Ag material residues remained in the laser-removed areas but some around the Ag grid line edges. The obvious changes of the Ag grid line-width could also be observed from these images. The insets in Fig. 10a–d provide the partially enlarged SEM images for individual Ag grid lines of the corresponding Ag grid TCFs, from which the Ag grid line-widths and Ag material residues at the Ag grid line edges could be further determined. The changes in Ag grid line-width also led to variations in Ag material content per unit area that could affect the optical transmittance and electrical conductivity of the Ag grid TCFs. These will be subsequently analyzed in more detail.

Figure 11a presents the optical transmittance spectra of the Ag grid TCFs with different Ag grid line-widths within the 250–900 nm waveband. A clear observation was that the optical transmittance of the Ag grid TCFs exhibited a monotonically decreasing trend with the increase in Ag grid line-width. As revealed in Fig. 10, the Ag material content

per unit area on the TCF surface was increased with the increase of grid line-width, and thus the light scattering and reflection losses from Ag would be increased [56], which should be responsible for the decreased optical transmittance of the TCF. The average transmittance values of the Ag grid TCFs with different grid line-widths in the 380–780 nm visible waveband calculated using Eq. (1) are displayed in Fig. 11b. It was found that with the increase in Ag grid line-width from 70 to 110 μm , the average transmittance values of the Ag grid TCFs gradually dropped from 81.08% to 75.53%. Considering the scattering and reflection effects of the Ag grids on the incident light, it can be deduced that the higher the Ag material content per unit area (equivalent to the larger Ag grid line-width), the lower the average visible transmittance due to the more light scattering and reflection losses [57, 58]. This can provide a good explanation for the average transmittance variations of the Ag grid TCFs with Ag grid line-width.

Figure 11b also provides the variations of the measured sheet resistance for the Ag grid TCFs with different grid line-widths. The sheet resistance was

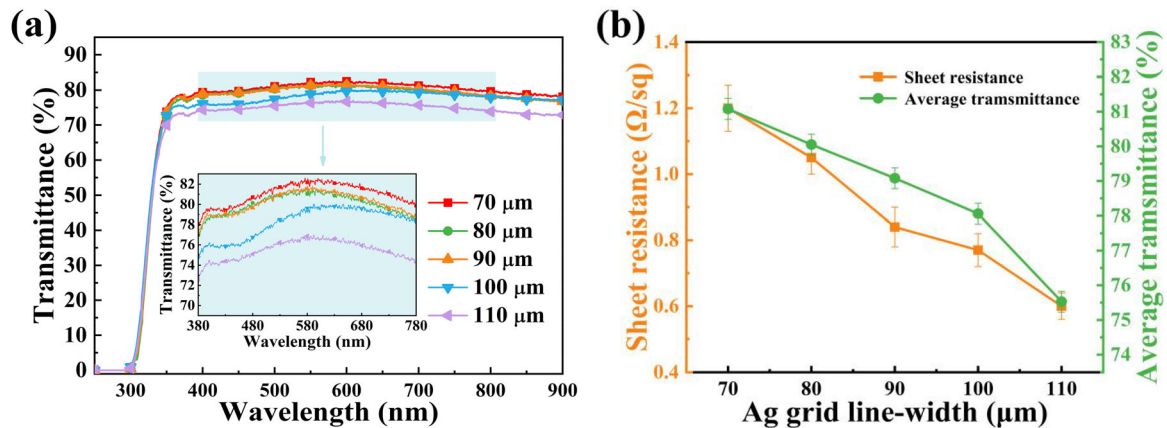


Fig. 11 **a** Optical transmittance spectra and **b** sheet resistance and average transmittance values of the Ag grid TCFs with different grid line-widths. The inset in **a** shows the optical transmittance spectra of the Ag grid TCFs in the visible waveband of 380–780 nm

observed to be monotonically decreased from 1.20 to 0.60 Ω/sq with the increase of Ag grid line-width from 70 to 110 μm . The reason for this result is similar to the previous analysis for the Ag grid pitch. The increase in Ag grid line-width implies the increase in Ag material content per unit area, which is undoubtedly conducive to the enhancement of the TCF electrical conductivity. Furthermore, it can be revealed from Eq. (2) that indeed the sheet resistance (R_{sh}) value of the Ag grid TCF is inversely proportional to the Ag grid line-width (b) under the fixed ρ , d , and l values. This can also corroborate the measured TCF sheet resistance values for the different Ag grid line-widths.

The above results demonstrate that an increased Ag grid line-width corresponds to an effectively dropped sheet resistance value and a remarkably degraded average transmittance value. Therefore, for the purpose of evaluating the comprehensive performances of the Ag grid TCFs with different grid line-widths, their F_{TC} values were also calculated using Eq. (3), and the results are given in Fig. 12. The grid line-width of 90 μm produced the highest F_{TC} value of $11.38 \times 10^{-2} \Omega^{-1}$, and the one of 110 μm gave rise to the lowest F_{TC} value of $10.07 \times 10^{-2} \Omega^{-1}$. This suggests that under the same other conditions, the optimal Ag grid line-width for fabricating an Ag grid TCF with the best comprehensive performance is 90 μm .

3.4 Influence of scanning method

It was determined that under the conventional LTCS method, using an Ag grid height of 800 nm, an Ag

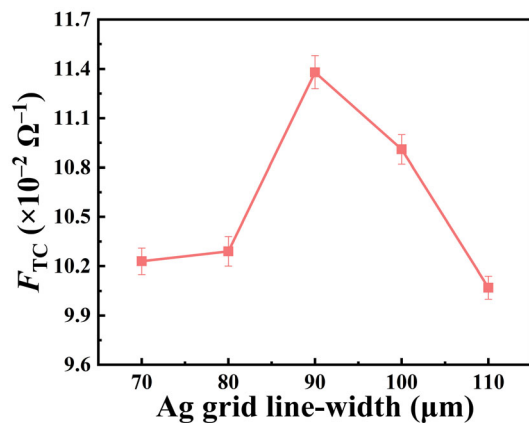


Fig. 12 Figure of merit (F_{TC}) values of the Ag grid TCFs with different grid line-widths

grid pitch of 1.0 mm and an Ag grid line-width of 90 μm can realize the fabrication of an Ag grid TCF with the best comprehensive performance. On the other hand, our previous work has proposed two new scanning (i.e., the aforementioned FTSS and FLCS) methods, which have been confirmed to be able to effectively improve the edge quality of the laser-removed areas and thus the optical transmittance of the SLA Ag patterns [31]. Therefore, the FTSS and FLCS methods were adopted here to further optimize the performances of the Ag grid TCFs under the optimal Ag grid parameters. Figure 13 provides the schematic diagrams of the conventional LTCS method as well as the proposed FTSS and FLCS methods. Briefly, the conventional LTCS method is featured by parallel lines, along which the laser beam will complete multiple single-track scans (Fig. 13a). The FTSS method is featured by a plurality of squares

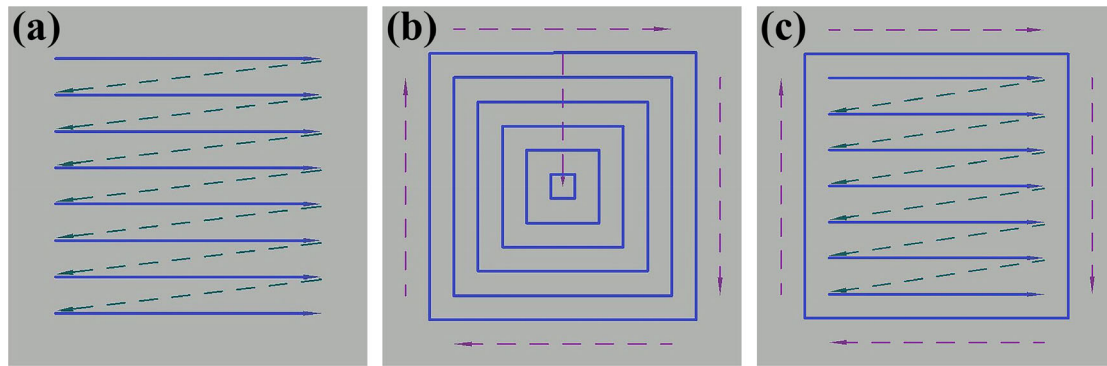


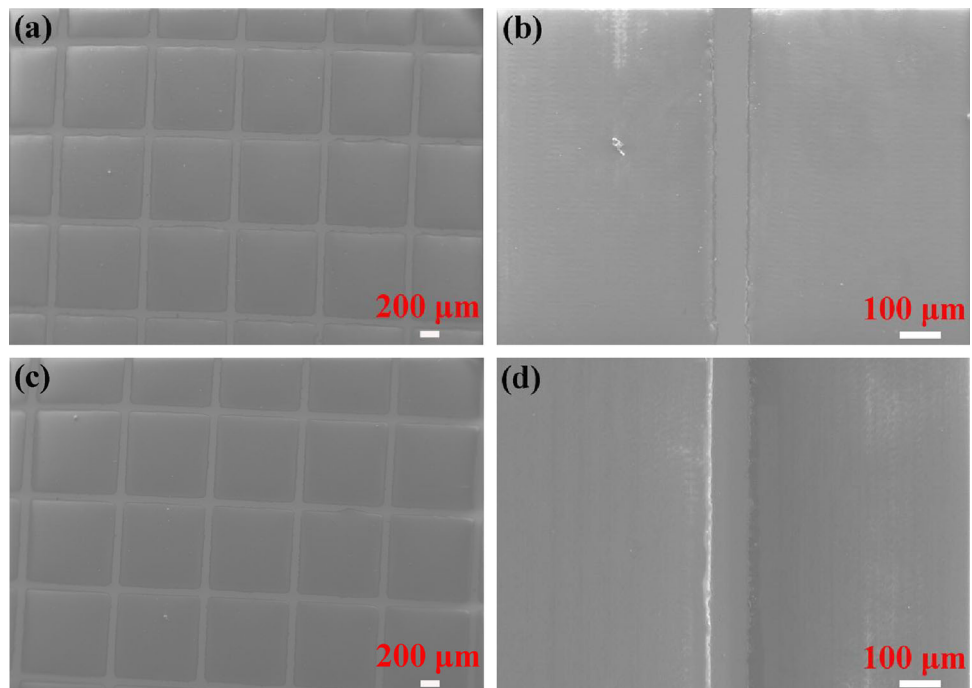
Fig. 13 Schematic diagrams of the three different scanning methods: **a** LTCS; **b** FTSS; **c** FLCS

or rectangles, along which the laser beam will complete multiple closed-loop scans from outside to inside (Fig. 13b). The FLCS method has a laser scanning path consisting of inner parallel lines that will be firstly completed and an outer square or rectangle that will be finally completed (Fig. 13c).

Figure 14 shows the low-magnification and partially enlarged SEM images of the Ag grid TCFs obtained under the scanning methods of FTSS and FLCS. Clear and regular Ag grid structures as well as clean laser-removed areas could be found on the two sample surfaces. Under the same grid parameters, the grid line-widths (90 μm) of the Ag grid TCFs fabricated using the FTSS and FLCS methods almost had no significant changes as compared to that using the

conventional LTCS method (Fig. 4). However, the Ag grid line edges became relatively smooth and flat and nearly no Ag material residues remained (Fig. 14b, d). These results should be related to the changes of the laser spot projection under different scanning methods [59]. During SLA, the removal of the Ag film is realized in the form of overlapping of circular laser pulses on the sample surface, and therefore the start and end regions of the laser removal path are usually semicircular [60, 61]. By contrast, the middle region of the laser removal path is relatively straight and smooth. When the conventional LTCS method is adopted, the laser spot stays longer at the start and end points (i.e., the grid line edges) compared with other points, thus causing a certain thermal effect on

Fig. 14 SEM images of the Ag grid TCFs fabricated using different scanning methods: **a** FTSS; **b** a partially enlarged view of **a**; **c** FLCS; **d** a partially enlarged view of **c**



both edges of the Ag grid line. Moreover, the semi-circular-shaped edges and the partial vaporization removal of the Ag film cause the formation of the Ag material residues at the Ag grid line edges [62], which will be detrimental to the comprehensive performance of the Ag grid TCF. Differently, in both cases of using the FTSS and FLCS methods, the relatively straight and smooth middle region of the laser removal path can be fully utilized to obtain ideal peripheral contours of the laser-removed areas. As a result, the laser action time at the Ag grid line edges can be effectively shortened, and the semicircular-shaped Ag grid line edges can be effectively eliminated. The resulting Ag grid line edges can thus be relatively smooth and flat without obvious Ag material residues, giving rise to the possibility of improving the optical and electrical properties of the corresponding Ag grid TCF [63].

Figure 15a presents the optical transmittance spectra of the Ag grid TCFs obtained under different scanning methods within the 250–900 nm waveband. It could be observed that the transmittance data of the TCFs under the FTSS and FLCS methods were obviously higher than that under LTCS. This should be mainly attributed to the new scanning methods which can significantly reduce the Ag material residues at the Ag grid line edges. The corresponding average transmittance values in the 380–780 nm visible waveband calculated using Eq. (1) are displayed in Fig. 15b for further quantitative comparison. It could be seen that the average transmittance of the Ag grid TCF obtained under the conventional LTCS method was 79.08%. The FTSS and FLCS methods

enabled the Ag grid TCFs to achieve obvious increases in average transmittance value, respectively, to 80.15% and 80.52%, which exhibited more than 1% increases as compared to the conventional LTCS method. As indicated earlier, the Ag material itself has strong scattering and reflection effects on the incident light that can cause a certain optical transmittance loss [53, 64]. Since the FTSS and FLCS methods are beneficial for effectively reducing the Ag material residues at the grid line edges, as confirmed from the SEM images in Fig. 14, the optical transmittance losses caused by scattering and reflection effects from the Ag material residues should certainly be much fewer as compared with that in the case of adopting the conventional LTCS method.

Figure 15b also provides the comparison among the measured sheet resistance values for the Ag grid TCFs obtained under different scanning methods. The sheet resistance values of the Ag grid TCFs obtained under the FTSS and FLCS methods were, respectively, increased to 0.90 Ω/sq and 0.88 Ω/sq as compared with that under the conventional LTCS method (0.84 Ω/sq), indicating that the electrical conductivity was slightly deteriorated. This is believed to be originated from the reduction of Ag material residues at the grid line edges [20, 65]. In the case of using the conventional LTCS method, the presence of the more Ag material residues that are connected with the Ag grid lines will result in decreased lengths of electron transportation paths and thus reduced chances of carrier recombination, which should be conducive to improving the TCF electrical conductivity. In comparison, the fewer Ag

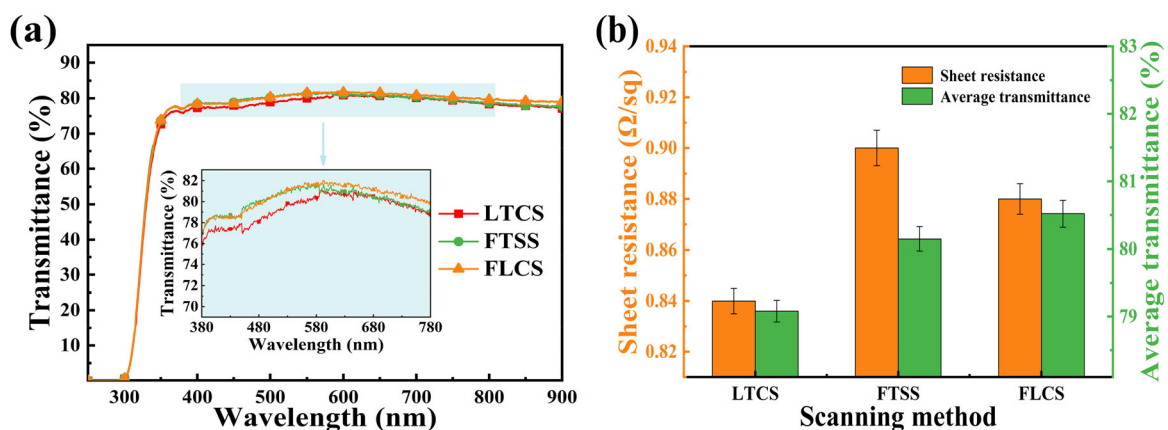


Fig. 15 **a** Optical transmittance spectra and **b** sheet resistance and average transmittance values of the Ag grid TCFs fabricated using different scanning methods. The inset in **a** shows the optical

transmittance spectra of the Ag grid TCFs in the visible waveband of 380–780 nm

material residues in the cases of using the FTSS and FLCS methods may make the TCF electrical conductivity weakened, which is manifested as the slight increases in sheet resistance.

The above results reveal that the new FTSS and FLCS methods can result in effectively improved optical transmittance but slightly degraded electrical conductivity of the Ag grid TCFs. Therefore, it is necessary to evaluate the comprehensive performances of the Ag grid TCFs obtained under the three scanning methods through calculating their F_{TC} values using Eq. (3). The calculated results are given in Fig. 16a. It could be determined that both the F_{TC} values of the Ag grid TCFs obtained under the FTSS and FLCS methods ($12.16 \times 10^{-2} \Omega^{-1}$ and $13.02 \times 10^{-2} \Omega^{-1}$) were obviously higher than that under the conventional LTCS method ($11.38 \times 10^{-2} \Omega^{-1}$). These results imply that the application of the new FTSS and FLCS methods can further optimize the comprehensive performance of the Ag grid TCF, and the Ag grid TCF has the best comprehensive performance under the FLCS method. Moreover, the as-obtained Ag grid TCFs exhibit much better comprehensive performances than the commercial ITO film ($T_{av} \geq 80\%$, $R_{sh} \leq 10 \Omega/\text{sq}$, $F_{TC} \geq 1.07 \times 10^{-2} \Omega^{-1}$) and can well meet the application requirements.

Figure 16b presents a comparison of the optical transmittance values at 550 nm and sheet resistance values of the Ag grid TCFs obtained under the FTSS and FLCS methods with those in other studies [21–24, 66, 67]. It can be seen that the best performance of the sample prepared in this present work surpasses those of the TCFs obtained by other

methods previously reported, such as lithography, nanoimprinting, crackle template, and inkjet printing. On the other hand, the fabrication time of the Ag grid TCF samples obtained under the FTSS and FLCS methods is about 24 and 29 min, respectively. By contrast, the fabrication of the TCF samples by lithography [21], nanoimprinting [22], crackle template [23], and inkjet printing [67] reported in other works takes up to about 25 min, more than an hour, half an hour, and more than two hours, respectively. These reveal that the proposed SLA process combined with the FTSS or FLCS method can not only fabricate Ag grid TCFs with more excellent performances, it also possesses a relatively higher fabrication efficiency. In addition, the proposed process for fabricating the Ag grid TCFs is relatively simple and free from expensive tools/materials (such as mask, template, and metal nanoparticle ink). It is worth mentioning that both the FTSS and FLCS methods can improve the properties of the Ag grid TCFs, but the FLCS method brings about a better comprehensive performance and takes less time than the FTSS method. From these aspects, the proposed SLA process combined with the FLCS method has a great prospect in efficiently fabricating high-performance metal grid TCFs in the future.

4 Conclusion

Ag grid TCFs were fabricated by SLA of the sputtered Ag films on glass substrates using different Ag grid heights, pitches, line-widths, and scanning

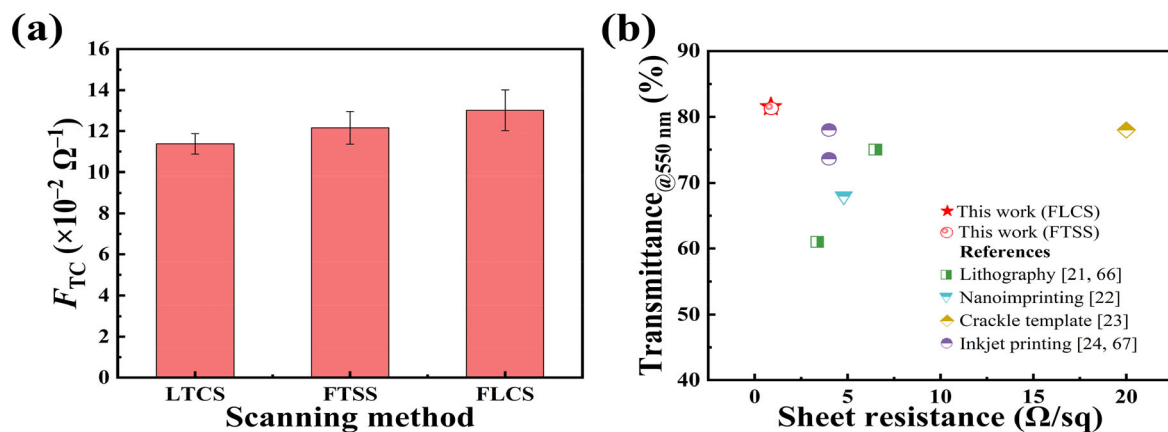


Fig. 16 a Figure of merit (F_{TC}) values of the Ag grid TCFs fabricated using different scanning methods. **b** Optical transmittance values at 550 nm versus sheet resistance values of

the Ag grid TCFs fabricated using the FTSS and FLCS methods, in comparison with those of the TCFs in other researches (reference numbers indicated)

methods. The SEM images confirmed that under the conventional LTCS method, both edges of the Ag grid line were semicircular, and no obvious Ag material residues remained in the laser-removed areas but some around the Ag grid line edges. The average visible transmittance and sheet resistance values of the resulting Ag grid TCFs exhibited decreasing trends with the increase in Ag grid height or line-width, but an increasing trend with the increase of Ag grid pitch. The Ag grid TCF with a grid height of 800 nm, a grid pitch of 1.0 mm, and a grid line-width of 90 μm was found to possess the best comprehensive performance with a figure of merit of $11.38 \times 10^{-2} \Omega^{-1}$. Importantly, it was verified that further performance improvements of the Ag grid TCFs could be achieved by adopting the two new FTSS and FLCS methods. Under the FTSS and FLCS methods, the Ag grid line edges were relatively smooth and flat without obvious Ag material residues, thus resulting in effectively improved optical transmittance with slightly degraded electrical conductivity of the Ag grid TCFs. The TCF fabricated under the FLCS method showed the highest figure of merit of $13.02 \times 10^{-2} \Omega^{-1}$ with an average visible transmittance of 80.52% and a sheet resistance of 0.88 Ω/sq , which can well meet the performance requirements in solar cells. This work indicates the feasibility of SLA combined with the FLCS method for fabricating high-performance metal grid TCFs, and more studies on fabrication of TCFs from other metal materials on various substrates are awaiting to be further explored.

Author contributions

QX: formal analysis and writing—original draft. BL: conceptualization, writing—review and editing, supervision, and project administration. LH: validation, resources, and funding acquisition. HL: formal analysis and investigation. YW: validation.

Funding

This research was financially supported by the National Natural Science Foundation of China (Grant Nos. 51805220 and 61405078).

Data availability

All data generated or analyzed during this study are included in this published article.

Declarations

Conflict of interest The authors declare that they have no competing financial interests or personal relationships that could have appeared to influence the work reported in this paper.

References

1. J. Bhattacharya, A. Peer, P.H. Joshi, R. Biswas, V.L. Dalal, Blue photon management by inhouse grown ZnO: Al cathode for enhanced photostability in polymer solar cells. *Sol. Energy Mater. Sol. Cells* **179**, 95–101 (2018)
2. H.F. Guo, C.H. Ma, Z.W. Chen, X.G. Jia, Q.F. Cang, N.Y. Yuan, J.N. Ding, The fabrication of $\text{Cu}_2\text{BaSnS}_4$ thin film solar cells utilizing a maskant layer. *Sol. Energy* **181**, 301–307 (2019)
3. T.H. Bointon, S. Russo, M.F. Craciun, Is graphene a good transparent electrode for photovoltaics and display applications? *IET Circuits Devices Syst.* **9**, 403–412 (2015)
4. Y.C. Su, C.C. Chiou, V. Marinova, S.H. Lin, N. Bozhinov, B. Blagoev, T. Babeva, K.Y. Hsu, D.Z. Dimitrov, Atomic layer deposition prepared Al-doped ZnO for liquid crystal displays applications. *Opt. Quantum Electron.* **50**, 205 (2018)
5. S.S. Li, Y.L. Wang, B.J. Li, L.J. Huang, N.F. Ren, Copper/silver composite mesh transparent electrodes with low reflection for high-performance and low-voltage transparent heaters. *J. Alloys Compd.* **865**, 158877 (2021)
6. K.H. Kim, T.H. Lee, K.R. Son, T.G. Kim, Performance improvements in AlGaIn-based ultraviolet light-emitting diodes due to electrical doping effects. *Mater. Des.* **153**, 94–103 (2018)
7. M.A. Haque, A.D. Sheikh, X. Guan, T. Wu, Metal oxides as efficient charge transporters in perovskite solar cells. *Adv. Energy Mater.* **7**, 1602803 (2017)
8. B.J. Li, G.Y. Yang, L.J. Huang, T.Y. Wang, N.F. Ren, Effects of BN layer on photoelectric properties and stability of flexible Al/Cu/ZnO multilayer thin film. *Ceram. Int.* **46**, 14686–14696 (2020)
9. L.G. De Arco, Y. Zhang, C.W. Schlenker, K. Ryu, M.E. Thompson, C.W. Zhou, Continuous, highly flexible, and transparent graphene films by chemical vapor deposition for organic photovoltaics. *ACS Nano* **4**, 2865–2873 (2010)
10. T. Sanniccolo, M. Lagrange, A. Cabos, C. Celle, J.-P. Simonato, D. Bellet, Metallic nanowire-based transparent

- electrodes for next generation flexible devices: a review. *Small* **12**, 6052–6075 (2016)
11. Q. Zhou, J.-N. Kim, K.-W. Han, S.-W. Oh, S. Umrao, E.J. Chae, I.-K. Oh, Integrated dielectric-electrode layer for triboelectric nanogenerator based on Cu nanowire-mesh hybrid electrode. *Nano Energy* **59**, 120–128 (2019)
 12. M.-G. Kang, H.J. Park, S.H. Ahn, T. Xu, L.J. Guo, Toward low-cost, high-efficiency, and scalable organic solar cells with transparent metal electrode and improved domain morphology. *IEEE J. Sel. Top. Quantum Electron.* **16**, 1807–1802 (2010)
 13. M. Nagaraja, P. Raghu, H.M. Mahesh, J. Pattar, Structural, optical and urbach energy properties of ITO/CdS and ITO/ZnO/CdS bi-layer thin films. *J. Mater. Sci.* **32**, 8976–8982 (2021)
 14. T.Y. Wang, B.J. Li, N.F. Ren, L.J. Huang, H. Li, Influence of Al/Cu thickness ratio and deposition sequence on photoelectric property of ZnO/Al/Cu/ZnO multilayer film on PET substrate prepared by RF magnetron sputtering. *Mater. Sci. Semicond. Process.* **91**, 73–80 (2019)
 15. Q. Wang, B.J. Li, F. Toor, H. Ding, Novel laser-based metasurface fabrication process for transparent conducting surfaces. *J. Laser Appl.* **31**, 022505 (2019)
 16. Y.J. Li, M.Y. Wu, Y.T. Sun, S.H. Yu, High-performance flexible transparent conductive thin films on PET substrates with a CuM/AZO structure. *J. Mater. Sci.* **30**, 13271–13279 (2019)
 17. K. Feng, H. Zheng, D. Zhang, G. Yuan, L.-Y. Chang, Y. Chen, J. Zhang, Carbon nanotube supported PtOx nanoparticles with hybrid chemical states for efficient hydrogen evolution. *J. Energy Chem.* **58**, 364–369 (2021)
 18. A. Kumar, C. Zhou, The race to replace tin-doped indium oxide: Which material will win? *ACS Nano* **4**, 11–14 (2010)
 19. T. Kim, A. Canlier, G.H. Kim, J. Choi, M. Park, S.M. Han, Electrostatic spray deposition of highly transparent silver nanowire electrode on flexible substrate. *ACS Appl. Mater. Interfaces* **5**, 788–794 (2013)
 20. S.S. Li, Y.L. Wang, B.J. Li, L.J. Huang, N.F. Ren, Femtosecond laser selective ablation of Cu/Ag double-layer metal films for fabricating high-performance mesh-type transparent conductive electrodes and heaters. *Opt. Commun.* **483**, 126661 (2021)
 21. C.-T. Wang, C.-C. Ting, P.-C. Kao, S.-R. Li, S.-Y. Chu, Investigation of surface energy, polarity, and electrical and optical characteristics of silver grids deposited via thermal evaporation method. *Appl. Surf. Sci.* **360**, 349–352 (2016)
 22. M.-G. Kang, L.J. Guo, Nanoimprinted semitransparent metal electrodes and their application in organic light-emitting diodes. *Adv. Mater.* **19**, 1391–1396 (2007)
 23. S. Kiruthika, R. Gupta, A. Anand, A. Kumar, G.U. Kulkarni, Fabrication of oxidation-resistant metal wire network-based transparent electrodes by a spray-roll coating process. *ACS Appl. Mater. Interfaces* **7**, 27215–27222 (2015)
 24. S.M. Yang, Y.S. Lee, Y. Jang, D. Byun, S.-H. Choa, Electromechanical reliability of a flexible metal-grid transparent electrode prepared by electrohydrodynamic (EHD) jet printing. *Microelectron. Reliab.* **65**, 151–159 (2016)
 25. S. Hong, J. Yeo, G. Kim, D. Kim, H. Lee, J. Kwon, H. Lee, P. Lee, S.H. Ko, Nonvacuum, maskless fabrication of a flexible metal grid transparent conductor by low-temperature selective laser sintering of nanoparticle ink. *ACS Nano* **7**, 5024–5031 (2013)
 26. F. Zacharatos, M. Makrygianni, R. Geremia, E. Biver, D. Karnakis, S. Leyder, D. Puerto, P. Delaporte, I. Zergioti, Laser direct write micro-fabrication of large area electronics on flexible substrates. *Appl. Surf. Sci.* **374**, 117–123 (2016)
 27. L.J. Huang, G.M. Zhang, H. Li, B.J. Li, Y.Y. Wang, N.F. Ren, Selective laser ablation and patterning on Ag thin films with width and depth control. *J. Mater. Sci.* **31**, 4943–4955 (2020)
 28. D. Paeng, J.-H. Yoo, J. Yeo, D. Lee, E. Kim, S.H. Ko, C.P. Grigoropoulos, Low-cost facile fabrication of flexible transparent copper electrodes by nanosecond laser ablation. *Adv. Mater.* **27**, 2762–2767 (2015)
 29. R. Böhme, K. Zimmer, The influence of the laser spot size and the pulse number on laser-induced backside wet etching. *Appl. Surf. Sci.* **247**, 256–261 (2005)
 30. Z.Y. Jia, K. Zhao, W. Liu, L.C. Ding, Localized and precision removal of metal coating on engineering plastics using NC laser milling. *Opt. Precis. Eng.* **24**, 94–101 (2016)
 31. B.J. Li, H. Li, L.J. Huang, Y.L. Wang, S.S. Li, N.F. Ren, Improving edge quality and optical transmittance of Ag films on glass substrates by selective nanosecond pulsed laser ablation using various scanning methods. *J. Mater. Sci.* **30**, 13729–13739 (2019)
 32. L. Romoli, M.M.A. Khan, M. Valentini, Through-the-thickness selective laser ablation of ceramic coatings on soda-lime glass. *Opt. Laser Technol.* **90**, 113–121 (2017)
 33. D. Barman, B.K. Sarma, Thin and flexible transparent conductors with superior bendability having Al-doped ZnO layers with embedded Ag nanoparticles prepared by magnetron sputtering. *Vacuum* **177**, 109367 (2020)
 34. N. Formica, D.S. Ghosh, T.L. Chen, C. Eickhoff, I. Bruder, V. Pruneri, Highly stable Ag–Ni based transparent electrodes on PET substrates for flexible organic solar cells. *Sol. Energy Mater. Sol. Cells* **107**, 63–68 (2012)
 35. C.M. Silvestre, J.H. Hemmingsen, E.S. Dreier, J. Kehres, O. Hansen, Laser ablation of high-aspect-ratio hole arrays in tungsten for X-ray applications. *Microelectron. Eng.* **209**, 60–65 (2019)

36. H. Liu, W. Zhang, J.-T. Gau, Z. Shen, G. Zhang, Y. Ma, X. Wang, Microscale laser flexible dynamic forming of Cu/Ni laminated composite metal sheets. *J. Manuf. Processes* **35**, 51–60 (2018)
37. J. Lee, S. Kim, M. Lee, Micro-scale patterning of indium tin oxide film by spatially modulated pulsed Nd:YAG laser beam. *Appl. Surf. Sci.* **228**, 9107–9111 (2012)
38. H. Yu, H. Lee, J. Lee, H. Shin, M. Lee, Laser-assisted patterning of solution-processed oxide semiconductor thin film using a metal absorption layer. *Microelectron. Eng.* **88**, 6–10 (2011)
39. X. Jia, X. Zhao, Numerical study of material decomposition in ultrafast laser interaction with metals. *Appl. Surf. Sci.* **463**, 780–790 (2010)
40. P. Umenne, V.V. Srinivasu, Femtosecond-laser fabrication of micron and sub-micron sized S-shaped constrictions on high T_c superconducting $\text{YBa}_2\text{Cu}_3\text{O}_{7-x}$ thin films: ablation and lithography issues. *J. Mater. Sci.* **28**, 5817–5826 (2017)
41. H.-J. Kim, K.-W. Seo, Y.H. Kim, J. Choi, H.-K. Kim, Direct laser patterning of transparent ITO–Ag–ITO multilayer anodes for organic solar cells. *Appl. Surf. Sci.* **328**, 215–221 (2015)
42. C. Zhang, D.W. Zhao, D. Gu, H. Kim, T. Ling, Y.R. Wu, L.J. Guo, An ultrathin, smooth, and low-loss Al-doped Ag film and its application as a transparent electrode in organic photovoltaics. *Adv. Mater.* **26**, 5696–5701 (2014)
43. B.J. Li, Y.Y. Wang, L.J. Huang, H.D. Cao, Q. Wang, H. Ding, N.F. Ren, Influences of ultrasonic vibration on morphology and photoelectric properties of F-doped SnO_2 thin films during laser annealing. *Appl. Surf. Sci.* **458**, 940–948 (2018)
44. L.J. Huang, L. Zhao, B.J. Li, Y. Zhang, Y.L. Wang, Y.Y. Wang, N.F. Ren, J. Song, Improving optical and electrical performances of aluminum-doped zinc oxide thin films with laser-etched grating structures. *Ceram. Int.* **47**, 7994–8003 (2021)
45. A. Khan, S. Lee, T. Jang, Z. Xiong, C. Zhang, J. Tang, L.J. Guo, W.-D. Li, High-performance flexible transparent electrode with an embedded metal mesh fabricated by cost-effective solution process. *Small* **12**, 3021–3030 (2016)
46. J. van de Groep, P. Spinelli, A. Polman, Transparent conducting silver nanowire networks. *Nano Lett.* **12**, 3138–3144 (2012)
47. A.K. Pal, D.B. Mohan, Structural, morphological and optical properties of Ag–AgO thin films with the effect of increasing film thickness and annealing temperature. *Opt. Mater.* **48**, 121–132 (2015)
48. G. Haacke, New figure of merit for transparent conductors. *J. Appl. Phys.* **47**, 4086–4089 (1976)
49. B.J. Li, Y.Y. Wang, L.J. Huang, H.D. Cao, Q. Wang, N.F. Ren, H. Ding, Ultrasonic-vibration-assisted laser annealing of fluorine-doped tin oxide thin films for improving optical and electrical properties: overlapping rate optimization. *Ceram. Int.* **44**, 22225–22234 (2018)
50. Y. Jang, J. Kim, D. Byun, Invisible metal-grid transparent electrode prepared by electrohydrodynamic (EHD) jet printing. *J. Phys. D* **46**, 155103 (2013)
51. J. Jang, H.-G. Im, J. Jin, J. Lee, J.-Y. Lee, B.-S. Bae, A flexible and robust transparent conducting electrode platform using electroplated silver grid/surface-embedded silver nanowire hybrid structure. *ACS Appl. Mater. Interfaces* **8**, 27035–27043 (2016)
52. Y. Mouchaal, G. Louarn, A. Khelil, M. Morsli, N. Stephant, A. Bou, T. Abachi, L. Cattin, M. Makha, P. Torchio, J.C. Bernède, Broadening of the transmission range of dielectric/metal multilayer structures by using different metals. *Vacuum* **111**, 32–41 (2015)
53. T. Winkler, H. Schmidt, H. Flügge, F. Nikolayzik, I. Baumann, S. Schmale, T. Weimann, P. Hinze, H.-H. Johannes, T. Rabe, S. Hamwi, T. Riedl, W. Kowalsky, Efficient large area semitransparent organic solar cells based on highly transparent and conductive ZTO/Ag/ZTO multilayer top electrodes. *Org. Electron.* **12**, 1612–1618 (2011)
54. G. Fan, J. Hu, B. Yang, L. Jia, X. Liu, S. Liu, Ag nanoparticle enhanced flexible thin-film silicon solar cells. *J. Nanosci. Nanotechnol.* **17**, 3689–3694 (2017)
55. J.-A. Jeong, J. Kim, H.-K. Kim, Ag grid/ITO hybrid transparent electrodes prepared by inkjet printing. *Sol. Energy Mater. Sol. Cells* **95**, 1974–1978 (2011)
56. M.K. Roul, J. Beckford, B. Obasogie, K. Yarbrough, M. Bahoura, A.K. Pradhan, High-performance transparent film heater using random mesowire silver network. *J. Mater. Sci.* **29**, 21088–21096 (2018)
57. S.X. Jiang, D.G. Miao, J.T. Xu, S.M. Shang, X. Ning, P. Zhu, Preparation and characterization of shielding textiles to prevent infrared penetration with Ag thin films. *J. Mater. Sci.* **28**, 3542–3547 (2017)
58. A. Kuroda, R. Satoh, Y. Iwata, K. Yokota, K. Fujimoto, S. Ura, K. Kintaka, Development of Ag alloy thin film with both high reflectance and adhesion for high density opt-electronic module. *IEEE Trans. Compon. Packag. Technol.* **30**, 302–308 (2007)
59. Y.L. Wang, B.J. Li, S.S. Li, H. Li, L.J. Huang, N.F. Ren, Parameter optimization in femtosecond pulsed laser etching of fluorine-doped tin oxide films. *Opt. Laser Technol.* **116**, 162–170 (2019)
60. G. Tang, A. Abdolvand, Laser-assisted highly organized structuring of copper. *Opt. Mater. Express* **1**, 1425–1432 (2011)

61. P. Woerner, D. Blood, D. Mills, M. Sheplak, W.S. Oates, Quantifying the uncertainty of picosecond pulsed laser ablation in sapphire. *J. Manuf. Processes* **35**, 687–699 (2018)
62. M.E. Shaheen, J.E. Gagnon, B.J. Fryer, Studies on laser ablation of silicon using near IR picosecond and deep UV nanosecond lasers. *Opt. Lasers Eng.* **119**, 18–25 (2019)
63. B.J. Li, G.Y. Yang, L.J. Huang, W. Zu, N.F. Ren, Performance optimization of SnO₂: F thin films under quasi-vacuum laser annealing with covering a transparent PET sheet: a study using processing map. *Appl. Surf. Sci.* **509**, 145334 (2020)
64. I.-C. Chen, B.-Y. Cheng, W.-C. Ke, C.-H. Kuo, L.-C. Chang, Improved light reflectance and thermal stability of Ag-based ohmic contacts on p-type GaN with La additive. *Superlattices Microstruct.* **57**, 51–57 (2013)
65. Y.Y. Wang, B.J. Li, L.J. Huang, H.D. Cao, N.F. Ren, Photoelectric property enhancement of Ag/FTO thin films by fabricating antireflection grating structures using ultrasonic-vibration-assisted laser irradiation. *Appl. Surf. Sci.* **541**, 148449 (2021)
66. D.S. Ghosh, T.L. Chen, V. Pruneri, High figure-of-merit ultrathin metal transparent electrodes incorporating a conductive grid. *Appl. Phys. Lett.* **96**, 041109 (2010)
67. J. Kang, Y. Jang, Y. Kim, S. Cho, J. Suhr, B.H. Hong, J. Choi, D. Byun, An Ag-grid/graphene hybrid structure for large-scale, transparent, flexible heaters. *Nanoscale* **7**, 6567–6573 (2015)

Publisher's Note Springer Nature remains neutral with regard to jurisdictional claims in published maps and institutional affiliations.